Second-Order Discretization in Space and Time for Radiation-Hydrodynamics

Simon Bolding[a], Joshua Hansel[a], Jarrod D. Edwards[b], Jim E. Morel[a], Robert B. Lowrie[c]

[a]*Department of Nuclear Engineering, 337 Zachry Engineering Center, TAMU 3133, Texas A&M University, College Station, Texas, 77843*
[b]*Phenomenology and Sensor Science Department, Sandia National Laboratory, Albuquerque, NM*
[c]*Computational Physics Group CCS-2, Los Alamos National Laboratory, P.O. Box 1663, MS D413, Los Alamos, NM 87545*

Abstract

Second-order accurate discretizations for radiation-hydrodynamics are currently an area of great interest. Second-order methods used to solve the hydrodynamics equations and second-order methods used to solve the radiation transport equation often differ fundamentally, making it difficult to combine them in a second-order manner. Here, we present a implicit-explicit (IMEX) method for solving the 1-D equations of radiation-hydrodynamics that is second-order accurate in space and time. Our radiation-hydrodynamics model consist of the 1-D Euler equations coupled with a grey radiation S_2 approximation. Our RH method combines the MUSCL-Hancock method for solving the Euler equations with the TR/BDF2 time integration scheme and the linear-discontinuous Galerkin finite-element spatial discretization scheme for the S_2 radiation equations. The MUSCL-Hancock method is commonly used for hydrodynamic calculations and the linear-discontinuous Galerkin scheme is the standard for the S_n equations of radiative transfer. While somewhat similar, these schemes vary fundamentally with respect to the treatment of spatial slopes. We address the challenges inherent to coupling these different numerical methods and demonstrate how these challenges can be overcome. Using the method of manufactured solutions, we show that the method is second-order accurate in space and time for both the equilibrium diffusion and streaming limit, and we show that the method is capable of computing radiative shock solutions accurately by comparing our results with semi-analytic solutions.

1. Introduction

Radiation hydrodynamics (RH) describes thermal radiation propagating through a fluid and the effects of the radiation on the properties of that fluid. Second-order accuracy in time for radiation-hydrodynamics calculations is currently an area of considerable interest. Though detailed work has been done for time integration of radiation diffusion and transport [1, 2, 3, 4, 5, 6, 7], and likewise for fluid dynamics [8], research in second-order methods that couple the two has only recently been carried out [9, 10, 11]. Because of the dramatically different time scales of radiation diffusion/transport and fluid advection, RH calculations are usually treated using an implicit-explicit (IMEX) scheme [9, 10, 11]. In such algorithms, the fluid advection component, which changes at a much slower rate, is treated explicitly; whereas, the radiation diffusion and radiation energy exchange terms are treated implicitly.

Sekora and Stone developed a scheme for RH that uses second-order Godunov methods to achieve second-order accuracy in space and time. This scheme is entirely explicit so that the time step is limited by the more rapidly varying radiation time scale [12]. Sekora's method is intended for the relativistic regime characterized as $a_\infty/c < 0.1$, where a_∞ denotes the speed of sound of the material and c denotes the speed of light. In this case, the fluid and radiation time-scales are not dramatically different, and therefore, the Courant limit time-step constraint is not overly restrictive. However, for the non-relativistic regime, i.e. $a_\infty/c < .01$, bounding the time-step according to the radiation time-scale will force the time steps to be at least two orders of magnitude smaller than the fluid time-scale. Kadioglu has also developed a second-order accurate scheme for both low and high energy density RH problems [13, 14]. Accuracy is achieved by incorporating the explicit algorithm into the implicit iterations. While this provides a tight coupling between the explicit and implicit terms, it is computationally more expensive than standard IMEX schemes, since the explicit block is solved in each nonlinear iteration [13].

In this work, we derive, implement, and test a new IMEX scheme for solving the equations of radiation hydrodynamics that is second-order accurate

in both space and time. We consider a 1-D RH system that combines a 1-D slab model of compressible fluid dynamics with a grey radiation S_2 model, given by:

$$\frac{\partial \rho}{\partial t} + \frac{\partial}{\partial x}(\rho u) = 0, \tag{1a}$$

$$\frac{\partial}{\partial t}(\rho u) + \frac{\partial}{\partial x}(\rho u^2) + \frac{\partial}{\partial x}(p) = \frac{\sigma_t}{c} F_{r,0}, \tag{1b}$$

$$\frac{\partial E}{\partial t} + \frac{\partial}{\partial x}[(E+p)u] = -\sigma_a c\left(aT^4 - E_r\right) + \frac{\sigma_t u}{c} F_{r,0}, \tag{1c}$$

$$\frac{1}{c}\frac{\partial \psi^+}{\partial t} + \frac{1}{\sqrt{3}}\frac{\partial \psi^+}{\partial x} + \sigma_t \psi^+ = \frac{\sigma_s}{4\pi}cE_r + \frac{\sigma_a}{4\pi}acT^4 - \frac{\sigma_t u}{4\pi c}F_{r,0} + \frac{\sigma_t}{\sqrt{3}\pi}Eu, \tag{1d}$$

$$\frac{1}{c}\frac{\partial \psi^-}{\partial t} - \frac{1}{\sqrt{3}}\frac{\partial \psi^-}{\partial x} + \sigma_t \psi^- = \frac{\sigma_s}{4\pi}cE_r + \frac{\sigma_a}{4\pi}acT^4 - \frac{\sigma_t u}{4\pi c}F_{r,0} - \frac{\sigma_t}{\sqrt{3}\pi}Eu, \tag{1e}$$

where ρ is the density, u is the velocity, $E = \frac{\rho u^2}{2} + \rho e$ is the total fluid energy density, e is the specific internal energy density, T is the fluid temperature, E_r is the radiation energy density,

$$E_r = \frac{2\pi}{c}\left(\psi^+ + \psi^-\right), \tag{2}$$

F_r is the radiation energy flux,

$$F_r = \frac{2\pi}{\sqrt{3}}\left(\psi^+ - \psi^-\right) \tag{3}$$

and $F_{r,0}$ is an approximation to the comoving-frame flux,

$$F_{r,0} = F_r - \frac{4}{3}E_r u. \tag{4}$$

Note that if we multiply Eqs. ((1d)) and (1e) by 2π and sum them, we obtain the radiation energy equation:

$$\frac{\partial E_r}{\partial t} + \frac{\partial F_r}{\partial x} = \sigma_a c(aT^4 - E_r) - \frac{\sigma_t u}{c}F_{r,0}, \tag{5a}$$

and if we multiply Eq. (1d) by $\frac{2\pi}{c\sqrt{3}}$, multiply Eq. (1e) by $-\frac{2\pi}{c\sqrt{3}}$ and sum them, we get the radiation momentum equation:

$$\frac{1}{c^2}\frac{\partial F_r}{\partial t} + \frac{1}{3}\frac{\partial E_r}{\partial x} = -\frac{\sigma_t}{c}F_{r,0}. \tag{5b}$$

3

Note that Eqs. (5a) and (5b) are known as the P_1 radiation approximation and are completely equivalent to Eqs. (1d) and (1e) under a similarity transformation defined by the invertible mapping given by Eqs. (2) and (3).

Equations (1a) through (1e) are closed in our calculations by assuming an ideal equation of state (EOS):

$$p = \rho e(\gamma - 1),$$ (6a)

$$T = \frac{e}{C_v},$$ (6b)

where γ is the adiabatic index, and C_v is the specific heat. However, our method is compatible with any valid EOS.

Our RH method combines the MUSCL-Hancock method (MHM) for solving the Euler equations with the TR/BDF2 time discretization scheme and the linear-discontinuous Galerkin finite-element (LDGFEM) spatial discretization scheme for the S_2 equations. The MUSCL-Hancock method is commonly used for hydrodynamic calculations and the linear-discontinuous Galerkin scheme is the standard for the S_n radiation equations. While somewhat similar, these schemes vary fundamentally with respect to the treatment of spatial slopes. The resolution of conflicts arising from these disparate slope treatments is a major component of our new RH method.

One of the most common methods for discretizing the S_n equations in time is the Crank-Nicolson method, also known as the Trapezoid Rule. This is a well-known, implicit method that is second-order accurate; however, its principal drawback is that it can become highly oscillatory for stiff systems. An alternative to this is a linear-discontinuous Galerkin method in time. Despite the fact that this scheme is more accurate than the Crank-Nicolson method and damps oscillations quickly, it has a much higher computational cost that is roughly equivalent to that of solving two Crank-Nicolson systems simultaneously over each time step. In this work, we use the TR/BDF2 scheme for discretizing the radiation S_2 and energy exchange terms in time. The TR/BDF2 scheme is a one-step, two-stage[1] implicit method that was first derived in [15]. There is actually a family of such schemes, but one member of the family can be shown to be optimal in a certain sense. A simple version of this method that is near-optimal was applied to the equations of

---

[1]Here we use the term "stage" to refer to an implicit equation that must be solved within each time step in a discretization scheme.

radiative transfer in [16], where it is shown to be both L-stable, accurate, and efficient. In [16], the near-optimal TR/BDF2 scheme is used to solve the equations of radiative transfer. It consists of a Crank-Nicolson step over half the time step and, using that solution, a BDF2 step over the remainder of the time step. The TR/BDF2 method has a computational cost that is roughly equivalent to that of solving two Crank-Nicolson systems sequentially over each time step. Here we introduce an alternative form of of the simple TR/BDF2 method that is particularly useful for our purposes.

A critical issue for radiation transport spatial discretizations is the preservation of the diffusion limit. Radiation-hydrodynamics problems often contain highly diffusive regions. In any type of calculation it is generally expected that accurate solutions will be obtained whenever the spatial variation of the solution is well-resolved by the mesh. However, use of a consistent transport discretization scheme in a highly diffusive problem will not guarantee such behavior. To ensure it, a consistent discretization scheme must "preserve" the diffusion limit or "be asymptotic preserving" [17]. A consistent discretization that does not preserve the diffusion limit will only yield accurate results in highly diffusive problems if the spatial cells are small with respect to a mean-free-path. Since the diffusion length can a arbitarily large with respect to a mean-free-path, discretization schemes that are not asymptotic preserving can be prohibitively expensive to use in problems with highly diffusive regions due to the need to arbitrarily over-resolve the solution. Thus preservation of the radiation diffusion limit is an essential property of any radiation-hydrodynamics scheme. Although we only use an S_2 radiation treatment, our overall coupling and solution scheme is applicable to an S_n treatment of arbitrary order. The only caveat is that a higher order S_n model will require a standard iterative solution technique for the S_n equations themselves rather than directly solving those equations as we do. An important aspect of our study is that we are able to investigate preservation of the diffusion limit assuming an LDFEM spatial discretization for a S_2 treatment that will be valid for an S_n treatment of arbitrary order.

The MHM includes spatial differencing for the advection equations and incorporates a linear interpolation from cell-averaged values to compute the slopes. However, Lowrie and Morel show in [18] that interpolation schemes which only depend on the mesh geometry and do not incorporate additional physical data, e.g. cross-section values, fail to have the diffusion limit. Furthermore, the differences in spatial discretization between the advection and S_2 equations present considerable complications due to the fact that, in the

5

MHM, the slopes are determined from interpolations of the cell-centered unknowns; whereas, in the LDFEM, the slopes are computed as part of the solution to the discretized spatial moment equations. To add to these complications, the internal energy of the fluid represents an unknown in both the fluid advection and radiation equations. The easy solution to this problem is to recompute the internal energy and radiation slopes at the beginning of each time step using the MHM limiter. Doing this, we were able to show that our method maintained the diffusion limit in 1D and reproduced shock solutions accurately. However, standard 2D and 3D hydrodynamics limiters use a spatial representation that will not maintain the radiation diffusion limit [19]. In particular, a simple linear dependence for the solution is assumed but a bilinear (2D) or a trilinear dependence (3D) is required [20]. Thus, to overcome this limitation, the method we present here retains the slopes computed by the LDFEM from one time step to the next. We use reconstructed slopes as determined in the MUSCL-Hancock method only to compute the advection fluxes, and we use the retained LDFEM slopes to initialize the implicit calculations for the radiation energy density and flux and for the fluid temperature update. This allows our method to reduce to its standard constituent methods when the contributions from coupled physics are negligible, and we believe it will also allow us to preserve the diffusion limit in a future extension of our method to 2D and 3D. Of course, this remains to be demonstrated.

The remainder of this paper is structured as follows. In Section 2, we give an overview of our second-order accurate radiation-hydrodynamics method, and we give a detailed description in the Appendix. In Section 3, we use the method of manufactured solutions to show that our method is second-order accurate in both space and time in the equilibrium diffusion limit as well as in the streaming limit. Then, in Section 4, we demonstrate the capability of our method to accurately compute radiation-hydrodynamic shocks by reproducing semi-analytic shock solutions. Finally, in Section 5, we summarize our results and present our conclusions and recommendations for future work.

2. Overview of the Radiation-Hydrodynamics Method

There are two cycles per time step. The first cycle spans the first half of the time step and the second spans the second half. The first cycle proceeds as follows:

1. Do a standard MHM predictor step.

2. Enter an iteration loop
   (a) Update the fluid momentum using lagged radiation momentum deposition
   (b) Simultaneously solve the total energy equation and the S_2 equations for the new radiation intensities and updated fluid internal energies using an LDG discretization in space and a Backward Euler discretization in time.
   (c) Continue the iteration until the fluid momenta, internal energies, and radiation intensities converge.
3. Do a standard MHM corrector step.
4. Initialize internal energy slopes to previous radiation solve values.
5. Enter an iteration loop
   (a) Update the fluid momentum using lagged radiation momentum deposition
   (b) Simultaneously solve the total energy equation and the S_2 equations for the new radiation intensities and updated fluid internal energies using an LDG discretization in space and a Crank-Nicolson discretization in time.
   (c) Continue iteration until the fluid momenta, internal energies, and radiation intensities converge.

The second cycle proceeds as follows:

1. Do a standard MHM predictor step.
2. Enter an iteration loop.
   (a) Update the fluid momentum using lagged radiation momentum deposition.
   (b) Simultaneously solve the total energy equation and the S_2 equations for the new radiation intensities and updated fluid internal energies using an LDG discretization in space and a Backward Euler discretization in time.
   (c) Continue iteration until fluid momenta, internal energies, and radiation intensities converge.
3. Do a standard MHM corrector step.
4. Initialize internal energy slopes to previous radiation solve values.
5. Enter an iteration loop
   (a) Update the fluid momentum using lagged radiation momentum deposition

(b) Simultaneously solve the total energy equation and the S_2 equations for the new radiation intensities and updated fluid internal energies using an LDG discretization in space and a BDF2 discretization in time.

(c) Continue iteration until fluid momenta, internal energies, and radiation intensities converge.

Note that the combination of Crank-Nicolson and BDF2 discretization results in a TR/BDF2 discretization over the full time step. We use a standard Backward Euler discretziaton for the radiation solves during the predictor stages, which only require first-order accuracy. One advantage to applying the full MHM over each half time step is that, if the time step size is being determined by the Courant limit, we can take twice the usual time step. In this case, the cost of four radiation solves per time step per iteration is mitigated. Alternatively, this algorithm could be viewed as a mixed, two-stage algorithm with alternating Crank-Nicolson and BDF2 solves over time steps (from this viewpoint, the time step sizes are governed by the standard Courant limit and there is only two radiation solves per time step).

Our scheme is designed in such a way that, if the radiation contributions to the hydrodynamics are negligible, the standard MHM solution is obtained over each half time step, and if the hydrodynamics contributions to the radiation diffusion are negligible, the standard TR/BDF2 solution for radiative transfer is obtained over the full time step. The process of iterating between the radiation momentum deposition to the fluid and the nonlinear radiation/internal energy solves is necessary to conserve total momentum. The radiation momentum deposition is usually small in the high energy density laboratory physics (HEDLP) regime, so a Picard-type iteration for the momentum deposition is adequate. In problems with stronger radiation momentum deposition, a better iteration scheme might be required.

2.1. Diffusion Limit

Of importance to obtaining the diffusion limit is using the correct initial internal energy slopes in the simultaneous solve for the S_2 intensities and the updated internal energies. Each MHM step provides slopes for the mass densities, the fluid momentum densities, and the fluid total energies. From the mass and fluid momentum slopes one can compute kinetic energy slopes. These slopes are used together with the fluid internal energy slopes determined from the previous-cycle radiation/internal energy solve to initialize the

8

left and right fluid total energies. A detailed description of how we modify the internal energy slopes can be found in Section Appendix B.3.

2.2. Slope limiting

McClarren and Lowrie [21] investigated the impact of slope limiting on asymptotic-preserving methods for hyperbolic systems with stiff relaxation terms that reduce to a parabolic description when relaxation dominates. This work is relevant to our radiation-hydrodynamics method. They found that a slope limiter must not introduce discontinuities at cell edges if asymptotic preservation is to be maintained. The minmod limiter has this property and is thus not suitable for radiation-hydrodynamics in general. However, the double minmod and the "sawtooth-free" limiter introduced by Lowrie do not have this property. Here we use the double minmod limiter.

2.3. Alternate Form of TBDF2 Method

Consider a partial differential equation of the form $\frac{\partial f}{\partial t} = \mathbf{A} f(t)$. We have derived the following non-standard form of the TR/BDF2 solution method to facilitate determining the form of the radiation coupling terms in the hydrodynamics equations:

$$\frac{2 \left(f^{n+1/2} - f^n \right)}{\Delta t} = \frac{1}{2}(\mathbf{A}f)^{n+1/2} + \frac{1}{2}(\mathbf{A}f)^n \,, \tag{7}$$

$$\frac{2 \left(f^{n+1} - f^{n+1/2} \right)}{\Delta t} = \frac{2}{3}(\mathbf{A}f)^{n+1} + \frac{1}{6}(\mathbf{A}f)^{n+1/2} + \frac{1}{6}(\mathbf{A}f)^n \,. \tag{8}$$

Note that each of these expression represents a conservation statement over each half time step. The usual expression that Eq. (8) replaces is

$$\frac{3 \left(f^{n+1} - f^{n+1/2} \right)}{\Delta t} - \frac{\left(f^{n+1/2} - f^n \right)}{\Delta t} = (\mathbf{A}f)^{n+1} \,, \tag{9}$$

which is clearly not a conservation statement. The MHM over each half-time step require a first-order accurate predictor stage. For the radiation coupling terms during the predictor stages, a standard Backward Euler discretization is used, e.g.,

$$\frac{2 \left(f^{n+1/2} - f^n \right)}{\Delta t} = (\mathbf{A}f)^{n+1/2} \,, \tag{10}$$

. Explicitly, Eq. (10) is used for the radiation/internal energy during the first and second cycle predictor steps. Eq. and the first cycle corrector step. Eq. (8) is used for the radiation/internal energy during the second cycle corrector step. This ensures total energy conservation over each time step.

9

3. Second-Order Accuracy for the Method of Manufactured Solutions

To demonstrate that our method is second-order accurate in space and time, we use the method of manufactured solutions (MMS). With MMS, we assume a functional form of the exact solution and derive extraneous sources for each equation that ensure the equations are satisfied analytically. We compare our numerical solution to the MMS problem to the exact solution as we refine the solution in space and time to examine to determine the order-accuracy of the algorithm. Two MMS problems, one for the streaming limit and one for the equilibrium diffusion limit, were taken from [22]. These solutions are composed of a combination of trigonometric functions with periodic boundary conditions. The solutions in [22] were modified to account for our S_2 model versus the P_1 radiation model. Additionally, our algorithm was implemented in a dimensionalized code, whereas the test problems are nondimensional.

An extraneous source is added to each equation in Eq. (**??**) to test the MMS problems. The analytic, dimensionalized forms of sources are determined from the resulting equations using symbolic computations, based on the chosen functional solution. These sources are then included in the discretized equations by evaluating spatial moments of the sources with high-accuracy quadrature. The sources are evaluated with the same time discretization of the appropriate step in the algorithm. We quantify the error between exact and numerical solutions using a relative L_2 norm of cell-averaged quantities, defined as

$$L_2^{\text{rel}}(u) = \sqrt{\sum_i^{N_x} (u_i - u_i^{\text{ex}})^2 \, \Delta x_i} \Bigg/ \sqrt{\sum_i^{N_x} (u_i^{\text{ex}})^2 \, \Delta x_i} \qquad (11)$$

where u is the quantity of interest and u_i^{ex} is the analytic solution averaged over the i-th spatial cell.

3.1. Accuracy in the Diffusion Limit

We have converted the nondimensional solutions in [22] to be compatible with our dimensionalized code. The problems are prescribed with two non-dimensional parameters

$$\mathbb{P} = \frac{aT_\infty^4}{\rho_\infty a_\infty^2}, \quad \mathbb{C} = \frac{c}{a_\infty}, \qquad (12)$$

10

where a_∞, T_∞, and ρ_∞ are the reference sound speed, material temperature, and density, respectively. There is not a unique mapping from the nondimensional solutions to a dimensional form. Thus, it is necessary to choose additional dimensional material parameters. We have chosen in our redimensionalization process to specify a reference material density that produces solutions with reasonable magnitudes. The values for cross sections, γ, $\mathbb{P}$, and $\mathbb{C}$ are taken from [22]. We then determine C_v and the remaining reference scalings from Eq. (12), Eq. (6a), and Eq. (6b). The non-dimensional solutions are redimensionalized by multiplying each variable by the appropriate reference scaling.

For the diffusion limit problem, the following dimensionalized solutions were prescribed for the hydrodynamic solution:

$$\rho = \rho_\infty \left(\sin(x - t) + 2 \right), \tag{13a}$$

$$u = a_\infty \frac{M}{2} \left(\cos(x - t) + 2 \right), \tag{13b}$$

$$p = \rho_\infty a_\infty^2 \alpha \left(\cos(x - t) + 2 \right), \tag{13c}$$

where α and M are constants. The factor $M/2$ was introduced to ensure that the material velocity is below sound speed. Using the perfect gas equation of state relations (Eq. (6b) and (6a)), an expression for material temperature T can be derived. The dimensionalized radiation energy density and flux are the following in the equilibrium diffusion limit:

$$E_r = aT^4, \tag{14a}$$

$$F_r = \frac{1}{3\sigma_t} \frac{\partial}{\partial x} acT^4 + \frac{4}{3} aT^4 u, \tag{14b}$$

Eqs. (2) and (3) are used to derive corresponding expressions for ψ^+ and ψ^- from the above expressions. Symbolic manipulation can then be used to derive the analytic MMS sources for each equation by substituting the solution into the left side of Eq. (1).

Following [22], we explore convergence of the solution as the cell optical thickness $\tau = \sigma \Delta x$ and $\mathbb{C}/\Delta x$ remain constant. This is to ensure that the solution remains diffusive, which would expose inaccuracy in methods that do not preserve the diffusion limit. As in [22], we use $\sigma = 10^5 \frac{N_x}{20}$ (cm^{-1}) and $\mathbb{C} = 10^5 \frac{N_x}{20}$, where N_x is the number of spatial cells for each simulation. The remaining problem specifications are $\rho_\infty = 1$ g cm^{-3}, $\alpha = 0.5$, $M = 0.9$, $\mathbb{P} =$

0.001, and $\gamma = \frac{5}{3}$. It is noted that because of how we have dimensionalized the solutions, the magnitude of reference parameters, and thus the solution, must change as $\mathbb{C}$ is modified. However, since our error norm is defined relative to the solution norm, we observe the proper convergence order. The simulation end time is 2π sh. The initial Δt is chosen based on a Courant condition of 0.6 to ensure stability of the MH algorithm. We then uniformly refine in space and time to demonstrate convergence in the two variables. It is worth noting that our initial time step size is chosen based on the Courant condition given in Eq. (B.1), which is based on material velocity speeds. This is a much larger and more physically reasonable time step size for an IMEX scheme than those in [22], which based the Courant condition on a non-dimensional speed of light. The nonlinear convergence of each implicit solve is set to 1.E-10 for all remaining simulations.

Figures B.1 and B.2 plots the error convergence as a function of Δx and Δt for internal energy and momentum, respectively. As demonstrated, the algorithm is second-order accurate in space and time for the equilibrium diffusion limit problem. Although not plotted here, second-order convergence was verified for E_r, F_r, and the other conserved and primitive hydrodynamic unknowns.

3.2. Streaming Limit

The second MMS problem corresponds to the streaming limit, in which the radiation and hydrodynamics are weakly coupled. In this limit, radiation streaming dominates relatively small radiation absorption and re-emission terms. Here, we keep the re-emission term small by making the opacity relatively small so that the radiation is nearly transparent to the fluid. Also, because the radiation streams much faster than the fluid, this results in a solution in which the unknowns evolve at significantly different time scales. The functional form of the streaming solutions are

$$\rho = \rho_\infty \left(\sin(x - t) + 2 \right) , \tag{15a}$$

$$u = a_\infty M \left(\cos(x - t) + 2 \right) , \tag{15b}$$

$$p = \rho_\infty a_\infty^2 \alpha \left(\cos(x - t) + 2 \right) , \tag{15c}$$

$$E_r = a T_\infty^4 \alpha \left(\cos(x - \mathbb{C}t) + 2 \right) \tag{15d}$$

$$F_r = a c T_\infty^4 \alpha \left(\cos(x - \mathbb{C}t) + 2 \right) \tag{15e}$$

12

Here, was can see that the wave speed of the radiation energy density is faster than that of the hydrodynamic unknowns by a factor of $\mathbb{C}$. This solution is also defined to mimic an isothermal flow regime, in which the radiation varies rapidly enough that changes in the fluid temperature are suppressed. In this case, the exact solution for the fluid temperature is a constant.

All problem parameters are fixed and then the space and time discretizations are refined uniformly. The problem is fully defined with the parameters $\mathbb{C} = 10$, $\mathbb{P} = 0.1$, $\rho_{infty} = 1$ g cm^{-3}, $\gamma = 5/3$, $\sigma_a = \sigma_t = 1$ cm^{-1}, $\alpha = 0.5$ and $M = 0.9$. The relatively high value of $\mathbb{P}$ and low value of $\mathbb{C}$ produce a more difficult problem to simulate, requiring convergence of the implicit solves. As before, the initial Δt is based on the Courant condition of 0.6. The simulation is performed until the initial radiation have advanced two periods, i.e., until $t = 4\pi/10$.

Figures B.3 and B.4 plots the error convergence as a function of Δx and Δt for internal energy and momentum, respectively. The convergence in the streaming limit is closer to 1.8 for the momentum variable. A finer time step size may be required to resolve the radiation unknowns more accurately than the Courant condition requires. The time step size may not yet be in the asymptotically converging region.

4. Results for Radiation-Hydrodynamic Shocks

Reproducing radiative shocks accurately, particularly in the optically thick regime, represents a challenging problem in the simulation of radiation hydrodynamics. A numerical scheme must be able to meet these challenges well. We will compare simulated steady state, radiative shocks to semi-analytical solutions [?]. The semianalytic solutions are based on a diffusion radiation model, which is equivalent to our S_2 radiation model at steady state. To reduce simulation times, we initialize the shocks with the analytic steady state solution projected onto the cell centered meshes and run the simulation until steady state is reached. At the boundary, we compute the fluxes using our standard Riemann solver, setting the hydrodynamic unknowns on the outside of the boundary equal to the far-stream conditions. Our algorithm will not be second-order globally due to the discontinuity at the shock [?]. Thus, we are not interested in order-accuracy here but are ensuring our code produce accurate solutions.

We test our algorithm for two radiative shocks, similar to those presented in [23], which incorporate a variety of structural features. For both shocks,

we set $\gamma = 5/3$, $c_v = 0.14472799784454$ Jks keV^{-1} g^{-1} (1 Jk= 10^9 J), and $\sigma_a = 577.35$ cm^{-1}. The problem specifications for the farstream pre and post-shock regions are provided in Table B.1. and Table **??** for the Mach 1.2 and Mach 3 shock, respectively. Results are generated with a CFL condition of 0.6 and $N_x = 500$ spatial cells.

First, we compute the Mach 1.2 shock, which has a hydrodynamic shock but no ISP. Fig. B.5 compare our results with the semi-analytic solutions for the fluid and radiation temperature. We see good agreement between the two. In this solution, we see a discontinuity in both the density and fluid temperature due to the hydrodynamic shock, and the maximum temperature is bounded by the far-downstream temperature, since there is no ISP to drive it further.

A Mach 3 shock is simulated that has both a hydrodynamic shock and an ISP. Fig. B.6 compares our numerical material and radiation temperature with the semi-analytic solutions. In each of these figures, we can see the effects of the hydrodynamic shock, causing a discontinuity in both the fluid density and temperature. We can also see the Zel'dovich spike, caused by the ISP embedded within the hydrodynamic shock, driving up the fluid temperature at the shock front. This spike leads to the relaxation region downstream as the fluid temperature and radiation temperature equilibrate. Here, we can see that our results still show very good agreement with the semi-analytic solution.

5. Conclusions and Future Work

We develop a new IMEX method for solving the equations of radiation-hydrodynamics that is second-order accurate in space and time. In addition to accuracy, we meet the goals outlined in Section 1: it reliably converges non-linearities, rapidly damps oscillations, incorporates modern algorithms used by the hydrodynamics and radiation transport communities, appears to have straightforward extensibility to a full radiation transport model, preserves the diffusion limit in 1D in such a way that it is expected to preserve this limit in 2D and 3D, accurately computes radiative shocks, and reduces to fundamental algorithms when the effects of coupled physics are negligible. Thus, it represents a very useful alternative to existing methods.

In future work, we recommend extending our radiation solver to incorporate a radiation transport model. The structure of our radiation-hydrodynamics algorithm should make this extension straightforward. Since

our algorithm only requires the angle-integrated radiation energy density and radiation current, the radiation solver may, in some sense, be treated as a black box module to compute these quantities. Of course, the angular intensities will need to be preserved across time steps. Momentum is already conserved by the chosen implicit statements. It is likely not necessary to fully converge the nonlinear solves in the predictor steps.

References

[1] R. G. McClarren, T. M. Evans, R. B. Lowrie, J. D. Densmore, Semi-Implicit Time Integration for Pn Thermal Radiative Transfer, Journal of Computational Physics 196 (2004) 566–590.

[2] R. B. Lowrie, A Comparison of Implicit Time Integration Methods for Nonlinear Relaxation and Diffusion, Journal of Computational Physics 196 (2004) 566–590.

[3] D. A. Knoll, R. B. Lowrie, J. E. Morel, Numerical Analysis of Time Integration Errors for Nonequilibrium Radiation Diffusion, Journal of Computational Physics 226 (2007) 1332–1347.

[4] G. L. Olson, Second-Order Time Evolution of Pn Equations for Radiation Transport, Journal of Computational Physics 228 (2009) 3027–3083.

[5] T. S. Axelrod, P. F. Dubois, C. E. R. Jr., An Implicit Scheme for Calculating Time- and Fequency-Dependent Flux Limited Radiation Diffusion in One Dimension, Journal of Computational Physics 54 (1984) 205–220.

[6] J. M. Stone, D. Mihalas, Upwind Monotonic Interpolation Methods for the Solution of the Time Dependent Radiative Transfer Equation, Journal of Computational Physics 100 (1992) 402–408.

[7] P. N. Brown, D. E. Shumaker, C. S. Woodward, Fully Implicit Solution of Large-Scale Non-equilibrium Radiation Diffusion with High Order Time Integration, Journal of Computational Physics 204 (2005) 760–783.

[8] E. Toro, Riemann Solvers and Numerical Methods for Fluid Dynamics: A Practical Introduction, Springer, 1999.

[9] R. B. Lowrie, J. E. Morel, J. A. Hittinger, The Coupling of Radiation and Hydrodynamics, Astrophysics Journal 521 (1999) 432–450.

[10] J. W. Bates, D. A. Knoll, W. J. Rider, R. B. Lowrie, V. A. Mousseau, On Consistent Time-Integration Methods for Radiation Hydrodynamics in the Equilibrium Diffusion Limit: Low-Energy-Density Regime, Journal of Computational Physics 167 (2001) 99–130.

[11] W. Dai, P. R. Woodward, Numerical Simulations for Radiation Hydrodynamics. I. Diffusion Limit, Journal of Computational Physics 142 (1998) 182–207.

[12] M. Sekora, J. Stone, A Higher Order Godunov Method for Radiation Hydrodynamics: Radiation Subsystem, Communication in Applied and Computational Mathematics 4 (2009) 135–152.

[13] S. Y. Kadioglu, A Second Order Self-Consistent IMEX Method for Radiation Hydrodynamics, Journal of Computational Physics 229 (2010) 8313–8332.

[14] S. Y. Kadioglu, A Fully Second Order Implicit/Explicit Time Integration Technique for Hydrodynamics Plus Nonlinear Heat Conduction Problems, Journal of Computational Physics 9 (2010) 3237–3249.

[15] R. E. Bank, W. M. Coughran, Jr., W. Fichtner, E. H. Grosse, D. J. Rose, R. K. Smith, Transient Simulation of Silicon Devices and Circuits, IEEE Transactions on Computer-Aided Design of Integrated Circuits and Systems 4 (1985) 436–451.

[16] J. D. Edwards, J. E. Morel, Nonlinear Variants of the TR/BDF2 Method for Thermal Radiative Diffusion, Journal of Computational Physics 230 (2011) 1198–1214.

[17] E. W. Larsen, J. E. Morel, J. W. F. Miller, Asymptotic Solutions of Numerical Transport Problems in Optically Thick, Diffusive Regimes, Journal of Computational Physics 69 (1987) 283–324.

[18] R. B. Lowrie, J. E. Morel, Issues with High-Resolution Godunov Methods for Radiation Hydrodynamics, Journal of Quantitative Spectroscopy & Radiative Transfer 69 (2001) 475–489.

[19] Z. J. Wang, High-order Methods for the Euler and NavierStokes Equations on Unstructured Grids, Progress in Aerospace Science 43 (2007) 1–41.

[20] M. L. Adams, Discontinuous Finite Element Transport Solutions in Thick Diffusive Problems, Nuclear Science and Engineering 137 (2001) 298–333.

[21] R. G. McClarren, R. B. Lowrie, The Effects of Slope Limiting on Asymptotic Preserving Numerical Methods for Hyperbolic Conservation Laws, Journal of Computational Physics 227 (2008) 9711–9726.

[22] R. G. McClarren, R. B. Lowrie, Manufactured Solutions for the P1 Radiation-Hydrodynamics Equations, Journal of Quantitative Spectroscopy & Radiative Transfer 109 (2008) 2590–2602.

[23] R. B. Lowrie, J. D. Edwards, Radiative Shock Solutions with Grey Non-equilibrium Diffusion, Shock Waves 18 (2008) 129–143.

[24] J. Morel, T. Wareing, K. Smith, Linear-Discontinuous Spatial Differencing Scheme for S_n Radiative Transfer Calculations, Journal of Computational Physics 128 (1996) 445–462.

Appendix A. Details of the Radiation-Hydrodynamics Method

Here we give a detailed description of our radiation-hydrodynamics method. First, we define some notation; the following are quantities stored throughout the calculation:

Radiation angular intensities	$\mathbf{R}^n \equiv \{\Psi_{i,L}^{\pm}, \Psi_{i,R}^{\pm}\} \quad \forall i$
Conservative hydrodynamics variables	$\mathbf{H}^n \equiv \{\rho_i^n, (\rho u)_i^n, E_i^n\} \quad \forall i$
MHM fluid internal energy slopes	$\delta e^n \equiv \{\delta e_i^n\} \quad \forall i$
MHM conservative variable slopes	$\bar{\Delta}^n \equiv \{\bar{\Delta}\rho_i^n, \bar{\Delta}(\rho u)_i^n, \bar{\Delta}E_i^n\} \quad \forall i$
Macroscopic cross sections	$\sigma^n \equiv \{\sigma_{s,i,L}^n, \sigma_{s,i,R}^n, \sigma_{a,i,L}^n, \sigma_{a,i,R}^n, \sigma_{t,i,L}^n, \sigma_{t,i,R}^n\} \quad \forall i$

Other quantities are computed when needed. The solution for a time step $t^n \to t^{n+1}$ consists of four nonlinear solves:

1. Crank-Nicolson step from t^n to $t^{n+\frac{1}{4}}$ (Cycle 1 Predictor)
2. Crank-Nicolson step from t^n to $t^{n+\frac{1}{2}}$ (Cycle 1 Corrector)
3. Crank-Nicolson step from $t^{n+\frac{1}{2}}$ to $t^{n+\frac{3}{4}}$ (Cycle 2 Predictor)
4. TR/BDF-2 step from $t^{n+\frac{1}{2}}$ to t^{n+1} (Cycle 2 Corrector)

1. **Perform Cycle 1 Predictor.**
   (a) **Perform MUSCL-Hancock Predictor.** First, slopes Δ^n are computed via Equations (B.4) and (B.5), optionally applying a slope limiter. Then a linear-discontinuous representation of the solution is created via Eq. (B.6), and the the MUSCL-Hancock predictor is performed to obtain $\mathbf{H}^*$, the homogeneous hydrodyamics solution at $t^{n+\frac{1}{4}}$, via Eq. (B.7).
   (b) **Perform nonlinear iterations.** Iteration of the $t^{n+\frac{1}{4}}$ solution is required since the system of equations is nonlinear.
      i. **Update velocities.** The Crank-Nicolson discretization of the velocity update equation, Eq. (B.9), is solved to obtain new velocities at cell centers, $\{u_i^{k+1}\}$. Evaluation of the radiation quantities E_r and F_r at cell centers is achieved by averaging the left and right values.
      ii. **Update radiation.** The Crank-Nicolson discretization of the S-2 equations, Equations (B.27) and (B.28) are solved, employing the linearization given in Section Appendix B.5. Evaluation of the densities and velocities at the edges is achieved

18

using using the cell-centered values in conjunction with the slopes Δ^n. Evaluation of the material energy E at edges is achieved using the internal energy slopes δe^n from a previous radiation solve. The computation of this slope is described in Section Appendix B.3.

iii. **Update internal energies.** The internal energies are updated in accordance with the linearization procedure given is Section Appendix B.5. The update equations produce edge values $\{e_{i,L}^{k+1}, e_{i,R}^{k+1}\}$. These left and right values are added to the kinetic energy at edges to produce cell-averaged values for the total energy $\{E_i^{k+1}\}$, which are used in the subsequent iteration. The values of δe are stored for the next radiation solve. Cross sections that are updated if they are functions of the hydrodynamic state of the fluid.

2. **Perform Cycle 1 Corrector.** This step proceeds just as the predictor step, except that the MUSCL-Hancock corrector step given by Eq. (B.8) is used instead of the MUSCL-Hancock predictor step, and the step goes from t^n to $t^{n+\frac{1}{2}}$ instead of t^n to $t^{n+\frac{1}{4}}$. No new hydrodynamic slopes are computed; evaluation of edge densities and velocities use Δ^n. However, evaluation of edge internal energies in the nonlinear iteration use $\delta e^{n+1/4}$. At the end of the cycle, the new internal energy slopes $\delta e^{n+\frac{1}{2}}$ are saved for the next cycle.

3. **Perform Cycle 2 Predictor.** This step proceeds just as the Cycle 1 predictor step, except that the step goes from $t^{n+\frac{1}{2}}$ to $t^{n+\frac{3}{4}}$ instead of t^n to $t^{n+\frac{1}{4}}$. As in Cycle 1, new slopes are computed in the MUSCL-Hancock predictor step; these slopes $\Delta^{n+\frac{1}{2}}$ are then used for evaluation of edge densities and velocities in the remainder of the cycle. Evaluation of edge internal energies and temperatures use the internal energies saved from the end of Cycle 1, $\delta e^{n+\frac{1}{2}}$.

4. **Perform Cycle 2 Corrector.** This step proceeds as the Cycle 1 corrector step, except that the time step goes from $t^{n+\frac{1}{2}}$ to t^{n+1}, and the time discretization of the equations is a form of TR/BDF-2 instead of Crank-Nicolson, so values at t^n are used in the temporal discretization. Slopes $\Delta^{n+\frac{1}{2}}$ and $\delta e^{n+\frac{3}{4}}$ are again used to evaluate edge quantities. At the end of the cycle, the new internal energy slopes δe^{n+1} are saved for the next cycle.

5. **Store values for next time step.** At this point, the old solutions, hydrodynamics slopes, internal energy slopes, and cross sections are

saved for the next time step.

Appendix B. The Time-Discretized Equations

In this section, we detail each of the equations for the MH solver and implicit radiation solves. The radiative transfer and hydrodynamic operators are treated independently via operator-splitting. Within the predictor and corrector stage of each cycle, there is an explicit hydrodynamic solve, followed by an associated implicit radiation solve. We will use a $*$ superscript to denote the intermediate operator-splitting states of variables resulting from the hydrodynamic steps.

Using a standard estimate of numerical wave speeds [8], our time step size for the n-th time step is estimated as

$$\Delta t^n = \max_i 2\text{CFL} \max_i \left(|u_i| + |a_{i,\infty}| \right) \tag{B.1}$$

where CFL is a chosen parameter, Δt is the full time step, and u_i and $a_{i,\infty}$ are the fluid velocity and sound speed for each cell i.

Appendix B.1. The MUSCL-Hancock Method

The MH solver handles the fluid advection portion of the RH equations by advancing the homogeneous Euler equations in time. The homogeneous Euler equations may be expressed in conservative form as

$$\frac{\partial \mathbf{H}}{\partial t} + \nabla \cdot \mathbf{F}(\mathbf{H}) = \mathbf{0} \,, \tag{B.2}$$

where $\mathbf{H}$ is a vector of the conservative unknowns and $\mathbf{F}(\mathbf{H})$ is the flux associated with each, i.e.,

$$\mathbf{H} = \begin{bmatrix} \rho \\ \rho u \\ E \end{bmatrix} \,, \qquad \mathbf{F}(\mathbf{H}) = \begin{bmatrix} \rho u \\ \rho u^2 + p \\ (E + p)u \end{bmatrix} \,. \tag{B.3}$$

There is a predictor and corrector MH step for each cycle. For example, the first predictor step advances the hydrodynamic unknowns from H^n to $H^{*,n+1/4}$. The predictor step begins by constructing a cell-wise linear representation of the solution using reconstructed slopes Δ_i^n:

$$\Delta_i^n = \frac{1}{2} \left(\Delta \mathbf{H}_{i-\frac{1}{2}}^n + \Delta \mathbf{H}_{i+\frac{1}{2}}^n \right) \,, \tag{B.4}$$

20

$$\Delta \mathbf{H}^n_{i-\frac{1}{2}} = \mathbf{H}^n_i - \mathbf{H}^n_{i-1}, \quad \Delta \mathbf{H}^n_{i+\frac{1}{2}} = \mathbf{H}^n_{i+1} - \mathbf{H}^n_i, \tag{B.5}$$

The slopes are modified using a double-minmod slope limiter to ensure positivity and stability [21]. A linear representation of the solution within each cell is then constructed as

$$\mathbf{H}^n_{i,L} = \mathbf{H}^n_i - \frac{\Delta^n_i}{2}, \quad \mathbf{H}^n_{i,R} = \mathbf{H}^n_i + \frac{\Delta^n_i}{2}, \tag{B.6}$$

This representation is then evolved by a quarter of a time step:

$$\mathbf{H}^{*n+\frac{1}{4}}_i = \mathbf{H}^n_i - \frac{\frac{1}{4}\Delta t}{\Delta x} \left(\mathbf{F}(\mathbf{H}^n_{i,R}) - \mathbf{F}(\mathbf{H}^n_{i,L}) \right). \tag{B.7}$$

At this point, an implicit Euler radiation solve advances the system from $t^{*,n+\frac{1}{4}}$ to $t^{n+\frac{1}{4}}$, as detailed in Sec. ??. Then, the corrector step of the MUSCL-Hancock method is applied. The corrector step employs an approximate Riemann solver to compute the fluxes based on the predicted hydrodynamic variables, i.e.,

$$\mathbf{H}^{*n+\frac{1}{2}}_i = \mathbf{H}^n_i - \frac{\Delta t}{\Delta x} \left(\mathbf{F}^{n+\frac{1}{4}}_{i+\frac{1}{2}} - \mathbf{F}^{n+\frac{1}{4}}_{i-\frac{1}{2}} \right), \tag{B.8}$$

where the fluxes are computed using an HLLC approximate Riemann solver [8]. At each edge, the Riemann solver uses linearly extrapolated values, based on lagged hydrodynamic slopes. For example, at the edge $x_{i-\frac{1}{2}}$, the Riemann solver computes fluxes with the states $\mathbf{H}^{n+1/4}_i - \frac{\Delta^n_i}{2}$ and $\mathbf{H}^{n+\frac{1}{4}}_{i-1} + \frac{\Delta^n_{i-1}}{2}$. The predictor and corrector steps for the second cycle proceed in the same manner.

Appendix B.2. The Iterative Radiation Solves

During each implicit radiation solve, the momentum deposition due to radiation and the energy exchange due to black-body emission must be iteratively solved. An outer fixed-point iteration is performed for the velocity update, with analytic Newton iterations for the radiative transfer terms. The equations below are for the $k + 1$-st iteration within each stage of the algorithm.

A lagged estimate of the radiation is used to compute a new material momentum. Noting that, in the absence of a momentum source, $\rho^{*,n+1/4} = \rho^{n+1/4}$. In the presence of MMS sources, ρ is updated prior to entering the iteration loops.

The BDF2 discretization of the velocity update equation is the following:

$$\frac{\rho_i^* \left(u_i^{k+1} - u_i^*\right)}{\Delta t} = \frac{1}{6} \left[\frac{\sigma_t}{c} \left(F_r - \frac{4}{3} E_r u\right)\right]_i^{n-1} + \frac{1}{6} \left[\frac{\sigma_t}{c} \left(F_r - \frac{4}{3} E_r u\right)\right]_i^n$$
$$+ \frac{2}{3} \left[\frac{\sigma_t}{c} \left(F_r - \frac{4}{3} E_r u\right)\right]_i^k .$$
(B.9)

The cell-averaged momentum source terms in these equations are computed by taking the linear average of the momentum source expressions evaluated at the edges, e.g.,

$$\left[\frac{\sigma_t}{c} \left(F_r - \frac{4}{3} E_r u\right)\right]_i = \frac{1}{2} \left[\frac{\sigma_{t,i,L}}{c} \left(F_{ri,L} - \frac{4}{3} E_{ri,L} u_{i,L}\right)\right]$$
$$+ \frac{1}{2} \left[\frac{\sigma_{t,i,R}}{c} \left(F_{ri,R} - \frac{4}{3} E_{ri,R} u_{i,R}\right)\right] . \quad \text{(B.10)}$$

. The Crank-Nicolson discretization of the velocity update equation is

$$\frac{\rho_i^* \left(u_i^{k+1} - u_i^*\right)}{\Delta t} = \frac{1}{2} \left[\frac{\sigma_t}{c} \left(F_r - \frac{4}{3} E_r u\right)\right]_i^n + \frac{1}{2} \left[\frac{\sigma_t}{c} \left(F_r - \frac{4}{3} E_r u\right)\right]_i^k . \quad \text{(B.11)}$$

The Backward-Euler discretizations for the predictor steps are analagously defined.

The lumped linear discontinuous discretization is used for the radiation equations, and thus inherently the update equations are uncoupled?. Thus, the hydrodynamic quantities need to be evaluated at cell edges. The stored solution values consist of the cell average unknowns for the conservative variables $[\rho, \rho u, E]$ and their slopes Δ, which were evaluated during a predictor step of the MUSCL-Hancock method, as given by Eq. (B.4). Evaluation of edge densities is achieved by applying the slopes as given by Eq. (B.6):

$$\rho_{i,L}^k = \rho_i^k - \frac{\Delta \rho_i^n}{2} . \quad \text{(B.12)}$$

Note that the slopes Δ are only updated in the MUSCL-Hancock predictor step. Evaluation of edge velocities is achieved based on the conservative variables ρ and ρu at edges, e.g.,

$$u_{i,L}^k = \frac{(\rho u)_{i,L}^k}{\rho_{i,L}^k} = \frac{(\rho u)_i^k - \frac{\Delta (\rho u)_i^n}{2}}{\rho_i^k - \frac{\Delta \rho_i^n}{2}} . \quad \text{(B.13)}$$

As explained in Section [Appendix B.3], internal energy unknowns, and thus material temperature, use slopes that are independent of the MUSCL-Hancock slopes. These internal energy slopes are denoted by δe. Evaluation of edge internal energies is thus performed as follows:

$$e_{i,L}^k = e_i^k - \frac{\delta e_i^n}{2} . \tag{B.14}$$

Again, quantities at t^{n+1} still use old slopes δe^n. These slopes are updated at the end of each full MUSCL-Hancock step, i.e., when the nonlinear iteration for the corrector step converges, the slopes δe_i^{n+1} are computed from the converged edge internal energies:

$$\delta e_i^{n+1} = e_{i,R}^{k+1} - e_{i,L}^{k+1} . \tag{B.15}$$

The Crank-Nicolson discretization of the energy update equation is

$$
\frac{E_{i,L}^{k+1} - E_{i,L}^*}{\Delta t} = -\frac{1}{2} \left[\sigma_a c \left(aT^4 - E_r \right) \right]_{i,L}^n - \frac{1}{2} \sigma_{a,i,L}^k c \left[aT^4 - E_r \right]_{i,L}^{k+1}
$$
$$
+ \frac{1}{2} \left[\sigma_t \frac{u}{c} \left(F_r - \frac{4}{3} E_r u \right) \right]_{i,L}^n + \frac{1}{2} \left[\sigma_t \frac{u}{c} \left(F_r - \frac{4}{3} E_r u \right) \right]_{i,L}^k . \tag{B.16}
$$

The right edge equations are identical in form, obtained by replacing "L" with "R" in the left edge equations. The BDF2 discretization of the energy update equation is

$$
\frac{E_{i,L}^{k+1} - E_{i,L}^*}{\Delta t} = -\frac{1}{6} \left[\sigma_a c \left(aT^4 - E_r \right) \right]_{i,L}^{n-1} - \frac{1}{6} \left[\sigma_a c \left(aT^4 - E_r \right) \right]_{i,L}^n
$$
$$
- \frac{2}{3} \sigma_{a,i,L}^k c \left[aT^4 - E_r \right]_{i,L}^{k+1} + \frac{1}{6} \left[\sigma_t \frac{u}{c} \left(F_r - \frac{4}{3} E_r u \right) \right]_{i,L}^{n-1}
$$
$$
+ \frac{1}{6} \left[\sigma_t \frac{u}{c} \left(F_r - \frac{4}{3} E_r u \right) \right]_{i,L}^n + \frac{2}{3} \left[\sigma_t \frac{u}{c} \left(F_r - \frac{4}{3} E_r u \right) \right]_{i,L}^k . \tag{B.17}
$$

The energy update to the Note that these energy update equations are not in the form in which they are actually solved in practice; the implicit term $\sigma_a^k a c (T^{k+1})^4$ must be linearized. The procedure for linearizing the thermal radiative transfer terms can be found in [24]. The final form of the energy update equation is a direct update to the edge internal energies $\{e_{i,L}^{k+1}, e_{i,R}^{k+1}\}$.

Appendix B.3. Using Radiation Internal Energy Slopes

As discussed in the introduction, the radiation solver and hydro solver use different internal energy slopes as an approach to preserve the equilibrium diffusion limit. The implementation of separate slopes is a proof of concept for higher dimensions. To mitigate confusion, in this section we will denote the hydro-state internal energy variables as e and the internal energy variables coming from the non-linear radiation solves as e^r. Care must be taken to ensure that total energy is conserved. The modified slopes are only applied to the implicit terms in each nonlinear solve.

During the MHM solve, we use the standard slope reconstruction formulas to advect variables to state U^* (or U^{**}), including total energy E. Then, in the non-linear iteration loop for the radiation and internal energy densities we use a modified slope for E^*, denoted ΔE^{r*}, that will preserve the diffusion limit. This ΔE^{r*} is based on the edge values of e^r of *the last iteration of the previous nonlinear radiation solve*. For example, if we are solving the cycle 1 corrector from state e^* to $e^{n+1/2}$, we use the edge values of e^r from the last iteration of the solve for $e^{r,n+1/4}$ to construct the slopes for $\Delta E^{r,*}$. The value of $\Delta E^{r,*}$ does not change over the duration of the nonlinear solve.

For the nonlinear solve we need the to use δe^r to construct ΔE^{*r} in the next solve (and thus the values $E_{R/L}^* = E_i^* \pm \frac{1}{2}\Delta E^{r*}$ needed for the LD radiation solve). We approximate this slope based on the hydro values for E^* as:

$$\Delta E^{r*} = E_R^{r*} - E_L^{r*} \tag{B.18}$$

where

$$E_R^{r*} = \rho_R^* \left((u_R^*)^2 + e_i^* + \delta e^{r,n+1/4} \right), \tag{B.19}$$

$$E_L^{r*} = \rho_R^* \left((u_L^*)^2 + e_i^* - \delta e^{r,n+1/4} \right), \tag{B.20}$$

and subscript i denotes cell average quantities. The edge values of ρ and u are evaluated using the MHM slopes as usual. Once we have completed the nonlinear solve for $e_{L/R}^{r,n+1/2}$, we must compute the change made to the cell-averaged total energy for the next MHM solve, such that total energy is conserved. The formula for the new total energy is

$$E_i^{n+1/2} = \frac{1}{2} \left[\rho_L \left(\frac{1}{2} u_L^2 + e_L^r \right) + \rho_R \left(\frac{1}{2} u_R^2 + e_R^r \right) \right]^{n+1/2} \tag{B.21}$$

where all variables are at time $t^{n+1/2}$. The internal energy slopes are computed and stored for the next nonlinear solve. For the first solve, the internal energy slopes are assumed zero.

24

Appendix B.4. S_2 Equations

A lumped linear discontinuous (LLD) spatial discretization is employed for the S_2 equations, so the angular flux unknowns are the left and right values $\Psi_{i,L}^{\pm}$ and $\Psi_{i,R}^{\pm}$ for each cell i. The spatially discretized equations result from integrating each half cell $(x_i - \frac{h_i}{2}, x_i)$ and $(x_i, x_i + \frac{h_i}{2})$, where x_i is the cell center, h_i is the cell width, and the cell average and edge fluxes are defined as

$$\Psi_i^{\pm} = \frac{1}{2}\left(\Psi_{i,L}^{\pm} + \Psi_{i,R}^{\pm}\right), \tag{B.22}$$

$$\Psi_{i+\frac{1}{2}}^{+} = \Psi_{i,R}^{+}, \qquad \Psi_{i+\frac{1}{2}}^{-} = \Psi_{i+1,L}^{-}. \tag{B.23}$$

Appendix B.4.1. Steady-State

Using an LLD discretization, the steady-state S_2 equations, obtained by dropping the $\frac{\partial \Psi^{\pm}}{\partial t}$ term in Eq. (**??**), become

$$\frac{2\mu^{\pm}}{h_i}\left(\Psi_i^{\pm,k+1} - \Psi_{i-\frac{1}{2}}^{\pm,k+1}\right) + \sigma_{t,i,L}^{k}\Psi_{i,L}^{\pm,k+1} - \frac{\sigma_{s,i,L}^{k}}{2}\phi_{i,L}^{k+1} = \mathcal{Q}_{i,L}^{\pm,k}, \tag{B.24}$$

$$\frac{2\mu^{\pm}}{h_i}\left(\Psi_{i+\frac{1}{2}}^{\pm,k+1} - \Psi_i^{\pm,k+1}\right) + \sigma_{t,i,R}^{k}\Psi_{i,R}^{\pm,k+1} - \frac{\sigma_{s,i,R}^{k}}{2}\phi_{i,R}^{k+1} = \mathcal{Q}_{i,R}^{\pm,k}. \tag{B.25}$$

Appendix B.4.2. Crank-Nicolson

$$\begin{aligned}
\frac{1}{c}\frac{\Psi_{i,L}^{\pm,k+1} - \Psi_{i,L}^{\pm,n}}{\Delta t} =\ & -\frac{1}{2}\frac{2\mu^{\pm}}{h_i}\left(\Psi_i^{\pm,n} - \Psi_{i-\frac{1}{2}}^{\pm,n}\right) - \frac{1}{2}\frac{2\mu^{\pm}}{h_i}\left(\Psi_i^{\pm,k+1} - \Psi_{i-\frac{1}{2}}^{\pm,k+1}\right) \\
& - \frac{1}{2}\sigma_{t,i,L}^{n}\Psi_{i,L}^{\pm,n} - \frac{1}{2}\sigma_{t,i,L}^{k}\Psi_{i,L}^{\pm,k+1} \\
& + \frac{1}{2}\frac{\sigma_{s,i,L}^{n}}{2}\phi_{i,L}^{n} + \frac{1}{2}\frac{\sigma_{s,i,L}^{k}}{2}\phi_{i,L}^{k+1} \\
& + \frac{1}{2}\mathcal{Q}_{i,L}^{\pm,n} + \frac{1}{2}\mathcal{Q}_{i,L}^{\pm,k}.
\end{aligned} \tag{B.26}$$

$$\frac{1}{c}\frac{\Psi_{i,R}^{\pm,k+1} - \Psi_{i,R}^{\pm,n}}{\Delta t} = -\frac{1}{2}\frac{2\mu^{\pm}}{h_i}\left(\Psi_{i+\frac{1}{2}}^{\pm,n} - \Psi_i^{\pm,n}\right) - \frac{1}{2}\frac{2\mu^{\pm}}{h_i}\left(\Psi_{i+\frac{1}{2}}^{\pm,k+1} - \Psi_i^{\pm,k+1}\right)$$
$$- \frac{1}{2}\sigma_{t,i,R}^{n}\Psi_{i,R}^{\pm,n} - \frac{1}{2}\sigma_{t,i,R}^{k}\Psi_{i,R}^{\pm,k+1}$$
$$+ \frac{1}{2}\frac{\sigma_{s,i,R}^{n}}{2}\phi_{i,R}^{n} + \frac{1}{2}\frac{\sigma_{s,i,R}^{k}}{2}\phi_{i,R}^{k+1}$$
$$+ \frac{1}{2}\mathcal{Q}_{i,R}^{\pm,n} + \frac{1}{2}\mathcal{Q}_{i,R}^{\pm,k} . \tag{B.27}$$

Appendix B.4.3. TR/BDF-2

$$\frac{1}{c}\frac{\Psi_{i,L}^{\pm,k+1} - \Psi_{i,L}^{\pm,n}}{\Delta t} = -\frac{1}{6}\frac{2\mu^{\pm}}{h_i}\left(\Psi_i^{\pm,n-1} - \Psi_{i-\frac{1}{2}}^{\pm,n-1}\right) - \frac{1}{6}\frac{2\mu^{\pm}}{h_i}\left(\Psi_i^{\pm,n} - \Psi_{i-\frac{1}{2}}^{\pm,n}\right)$$
$$- \frac{2}{3}\frac{2\mu^{\pm}}{h_i}\left(\Psi_i^{\pm,k+1} - \Psi_{i-\frac{1}{2}}^{\pm,k+1}\right)$$
$$- \frac{1}{6}\sigma_{t,i,L}^{n-1}\Psi_{i,L}^{\pm,n-1} - \frac{1}{6}\sigma_{t,i,L}^{n}\Psi_{i,L}^{\pm,n} - \frac{2}{3}\sigma_{t,i,L}^{k}\Psi_{i,L}^{\pm,k+1}$$
$$+ \frac{1}{6}\frac{\sigma_{s,i,L}^{n-1}}{2}\phi_{i,L}^{n-1} + \frac{1}{6}\frac{\sigma_{s,i,L}^{n}}{2}\phi_{i,L}^{n} + \frac{2}{3}\frac{\sigma_{s,i,L}^{k}}{2}\phi_{i,L}^{k+1}$$
$$+ \frac{1}{6}\mathcal{Q}_{i,L}^{\pm,n-1} + \frac{1}{6}\mathcal{Q}_{i,L}^{\pm,n} + \frac{2}{3}\mathcal{Q}_{i,L}^{\pm,k} , \tag{B.28}$$

$$\frac{1}{c}\frac{\Psi_{i,R}^{\pm,k+1} - \Psi_{i,R}^{\pm,n}}{\Delta t} = -\frac{1}{6}\frac{2\mu^{\pm}}{h_i}\left(\Psi_{i+\frac{1}{2}}^{\pm,n-1} - \Psi_i^{\pm,n-1}\right) - \frac{1}{6}\frac{2\mu^{\pm}}{h_i}\left(\Psi_{i+\frac{1}{2}}^{\pm,n} - \Psi_i^{\pm,n}\right)$$
$$- \frac{2}{3}\frac{2\mu^{\pm}}{h_i}\left(\Psi_{i+\frac{1}{2}}^{\pm,k+1} - \Psi_i^{\pm,k+1}\right)$$
$$- \frac{1}{6}\sigma_{t,i,R}^{n-1}\Psi_{i,R}^{\pm,n-1} - \frac{1}{6}\sigma_{t,i,R}^{n}\Psi_{i,R}^{\pm,n} - \frac{2}{3}\sigma_{t,i,R}^{k}\Psi_{i,R}^{\pm,k+1}$$
$$+ \frac{1}{6}\frac{\sigma_{s,i,R}^{n-1}}{2}\phi_{i,R}^{n-1} + \frac{1}{6}\frac{\sigma_{s,i,R}^{n}}{2}\phi_{i,R}^{n} + \frac{2}{3}\frac{\sigma_{s,i,R}^{k}}{2}\phi_{i,R}^{k+1}$$
$$+ \frac{1}{6}\mathcal{Q}_{i,R}^{\pm,n-1} + \frac{1}{6}\mathcal{Q}_{i,R}^{\pm,n} + \frac{2}{3}\mathcal{Q}_{i,R}^{\pm,k} , \tag{B.29}$$

26

*Appendix B.5. Linearization of Equations for General Temporal Discretiza-
tion*

Within each solution time step, first the hydro variables are advected
(either using local predicted fluxes or a Riemann solver). Then, a non-linear
system must be solved iteratively with iteration index k. Consider the case
of a non-linear system over a single step from t_n to t_{n+1}. We will combine all
known source terms as Q_k, which are known from previous states in time or
the previous iteration k. To linearize the system, we perform the standard
approach of linearizing the Planckian function about some temperature near
T^{n+1}, denoted T^k. For the initial iteration, $T^k = T^n$.

First, the original equation is rewritten as

$$\frac{E^{k+1} - E^*}{\Delta t} = -\alpha \left[\sigma_a^k c \left(a(T^{k+1})^4 - E_r^{k+1} \right) \right] + Q_E^k$$

where for BDF2,

$$Q_E^k = -\frac{1}{6} \left[\sigma_a c \left(aT^4 - E_r \right) \right]^{n-1} - \frac{1}{6} \left[\sigma_a c \left(aT^4 - E_r \right) \right]^n$$
$$+ \frac{1}{6} \left[\sigma_t \frac{u}{c} \left(F_r - \frac{4}{3} E_r u \right) \right]^{n-1} + \frac{1}{6} \left[\sigma_t \frac{u}{c} \left(F_r - \frac{4}{3} E_r u \right) \right]^n + \frac{2}{3} \left[\sigma_t \frac{u}{c} \left(F_r - \frac{4}{3} E_r u \right) \right]^k ,$$
$$\text{(B.30)}$$

for CN,

$$Q_E^k = -\frac{1}{2} \left[\sigma_a c \left(aT^4 - E_r \right) \right]^n$$
$$+ \frac{1}{2} \left[\sigma_t \frac{u}{c} \left(F_r - \frac{4}{3} E_r u \right) \right]^n + \frac{1}{2} \left[\sigma_t \frac{u}{c} \left(F_r - \frac{4}{3} E_r u \right) \right]^k , \quad \text{(B.31)}$$

and for BE,

$$Q_E^k = \sigma_t \frac{u}{c} \left(F_r - \frac{4}{3} E_r u \right)^k .$$

The scale factor α for BE, CN, and BDF2 is 1, $\frac{1}{2}$, and $\frac{2}{3}$, respectively. With
these definitions, the Planckian source term becomes

$$\sigma_a^k ac \left(T^{k+1} \right)^4 = \left(1 - \nu_\alpha^k \right) \sigma_a^k ac (T^k)^4 + \sigma_a^k c \nu_\alpha^k E_r^{k+1}$$
$$+ \frac{\nu_\alpha^k}{\alpha} Q_E^k - \frac{\rho \nu_\alpha^k}{\alpha \Delta t} \left[(e^k - e^*) + \frac{1}{2}((u^{k+1})^2 - (u^*)^2) \right] . \quad \text{(B.32)}$$

27

with

$$\nu_\alpha^k = \frac{\alpha \sigma_a c \Delta t \frac{\beta^k}{\rho}}{1 + \alpha \sigma_a c \Delta t \frac{\beta^k}{\rho}}. \tag{B.33}$$

and $\beta^k = \frac{4a(T^k)^3}{c_v^k}$. The energy update equation becomes

$$e^{k+1} = \alpha \frac{(1 - \nu_\alpha) \Delta t}{\rho} \left[\sigma_a^k c \left(E_r^{k+1} - a(T^k)^4 \right) + \frac{Q_E^k}{\alpha} \right]$$
$$- (1 - \nu_\alpha) \left(\frac{1}{2} [(u^{k+1})^2 - (u^*)^2] \right) + (1 - \nu_\alpha) e^* + \nu_\alpha e^k. \tag{B.34}$$

After solving for E_r^{k+1}, a new internal energy can be estimated using Eq. (B.35) to conserve energy. Momentum is only conserved to the tolerance of the velocity iterations. Iterations are repeated until convergence, beginning with a solve of Eq. (**??**) with updated radiation quantities. Once the system is converged, the EOS can be used to update p^{n+1}.
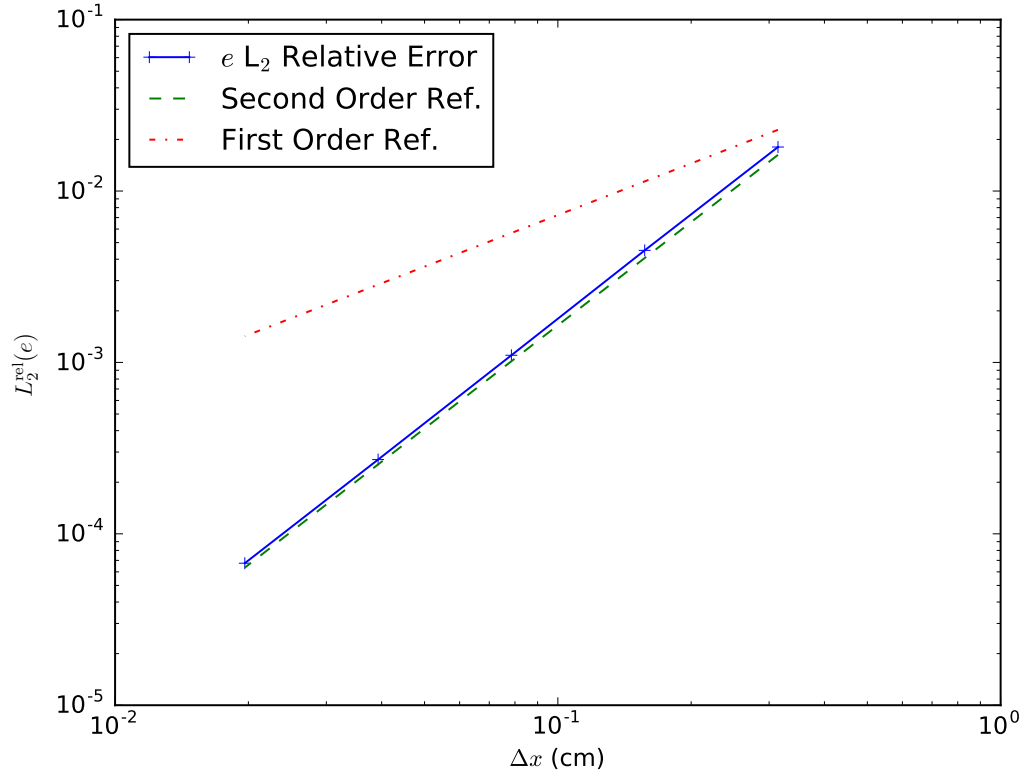
Figure B.1: Convergence of internal energy e in space for the equilibrium diffusion limit MMS problem
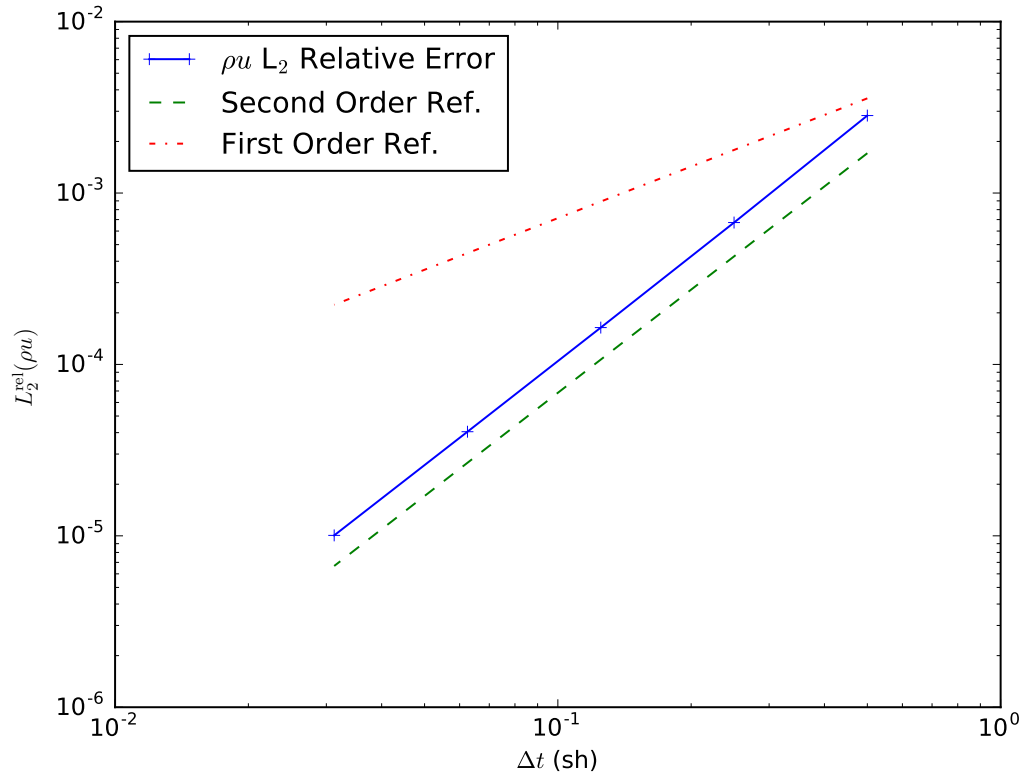
Figure B.2: Convergence of momentum ρu in time for the equilibrium diffusion limit MMS problem
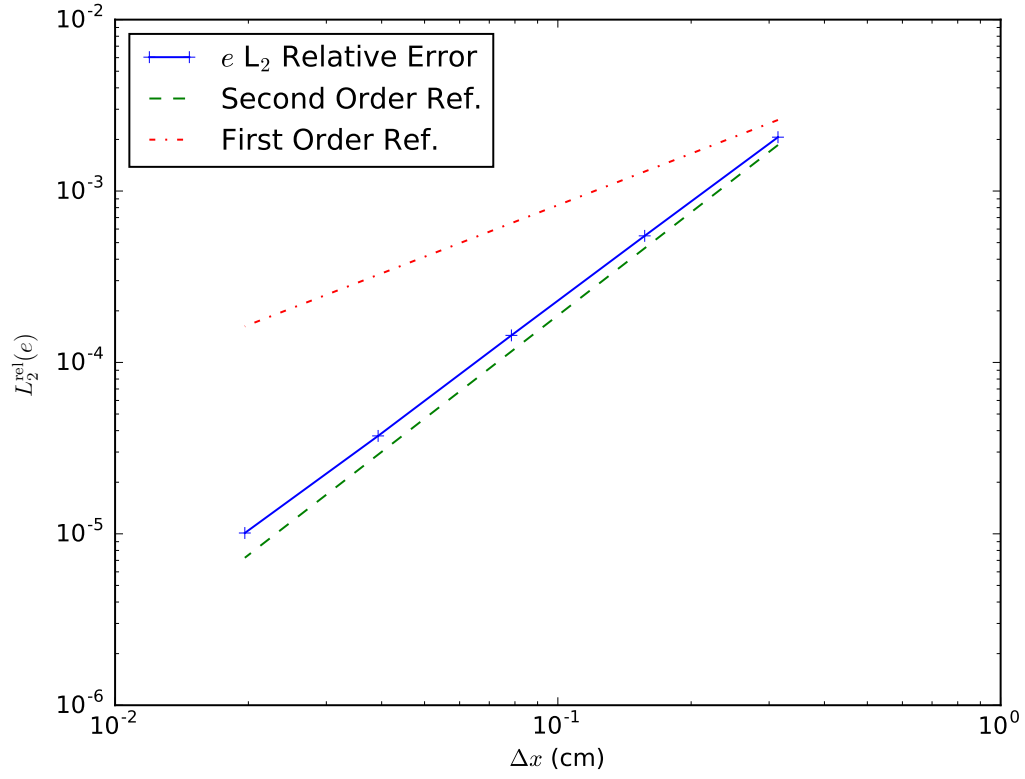
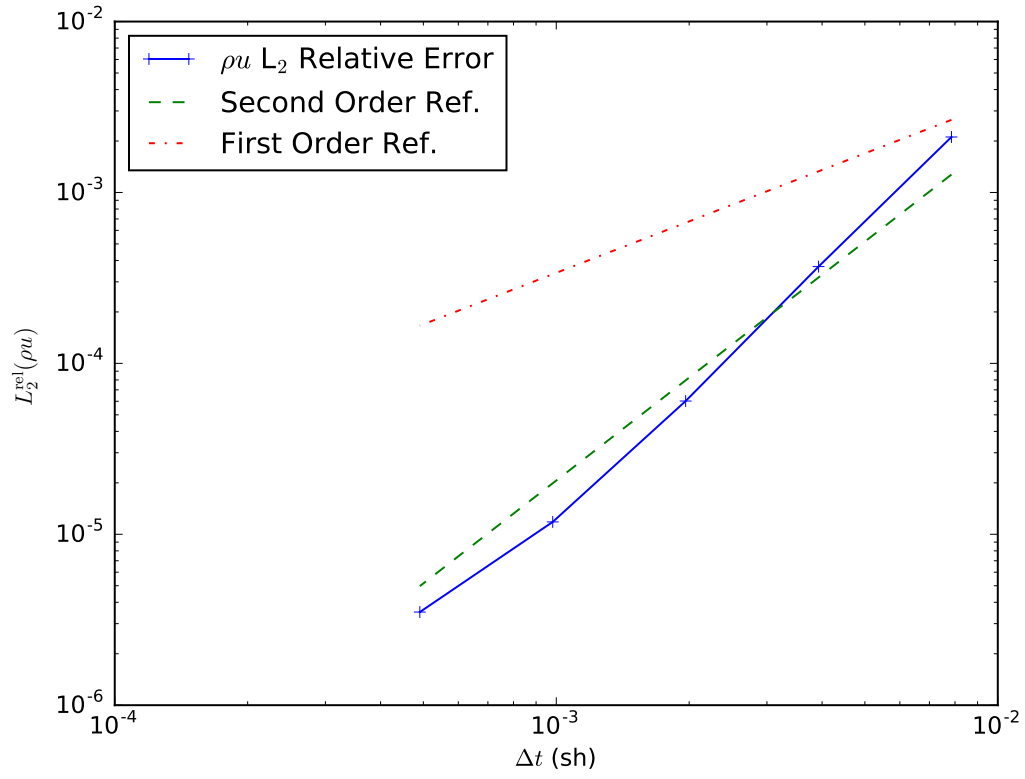Figure B.3: Convergence of internal energy e in space for the MMS streaming problem

Figure B.4: Convergence of momentum ρu in time for the MMS streaming problem
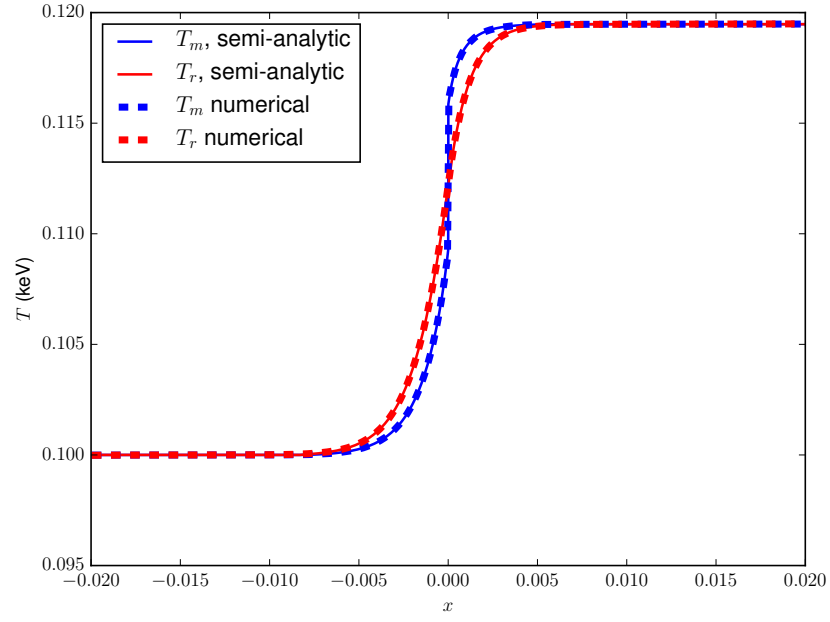
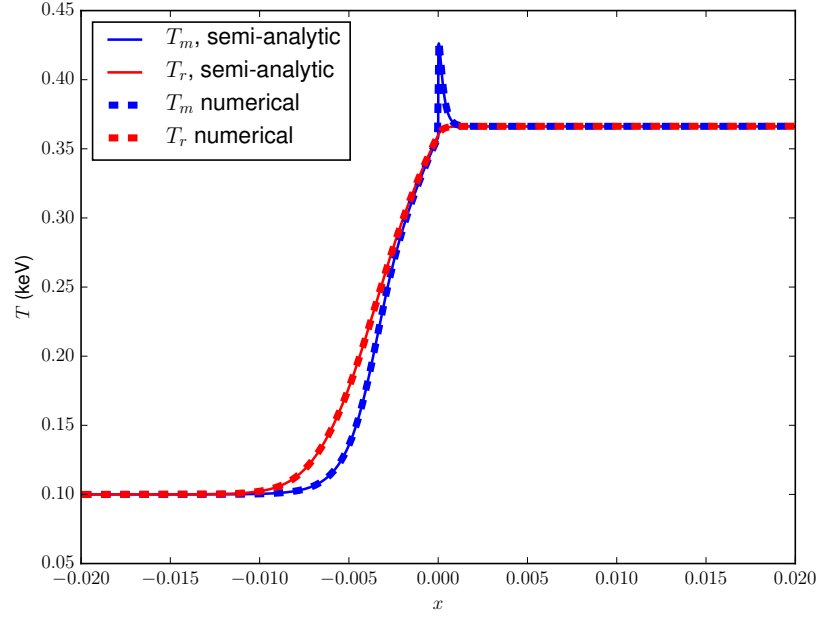Figure B.5: **Mach 1.2 radiative shock fluid and radiation temperatures.**

Figure B.6: **Mach 3.0 radiative shock fluid and radiation temperatures.**

Table B.1: Initial condition values for the Mach 1.2 radiative shock problem

Parameter	Pre-shock Value	Post-shock Value	Units
ρ	1.00000000e+00	1.29731782e+00	g cm^{-3}
u	1.52172533e-01	1.17297805e-01	cm sh^{-1}
T	1.00000000e-01	1.19475741e-01	keV
E	2.60510396e-02	3.13573034e-02	Jks cm^{-3}
E_r	1.37201720e-06	2.79562228e-06	Jks cm^{-3}
F_r	0.00000000e+00	0.00000000e+00	Jks cm^{-2} s^{-1}

Table B.2: Initial condition values for the Mach 3 radiative shock problem

Parameter	Pre-shock Value	Post-shock Value	Units
ρ	1.00000000e+00	3.00185103e+00	g cm^{-3}
u	3.80431331e-01	1.26732249e-01	cm sh^{-1}
T	1.00000000e-01	3.66260705e-01	keV
E	8.68367987e-02	1.83229115e-01	Jks cm^{-3}
E_r	1.37201720e-06	2.46899872e-04	Jks cm^{-3}
F_r	0.00000000e+00	0.00000000e+00	Jks cm^{-2} s^{-1}